

## Observation of the Anisotropic Magneto-Thomson Effect

Rajkumar Modak<sup>1,\*</sup>, Takamasa Hirai<sup>1</sup>, Seiji Mitani<sup>1</sup>, and Ken-ichi Uchida<sup>1,2,†</sup>

<sup>1</sup>National Institute for Materials Science, Tsukuba 305-0047, Japan

<sup>2</sup>Institute for Materials Research, Tohoku University, Sendai 980-8577, Japan

(Received 2 March 2023; revised 16 June 2023; accepted 16 October 2023; published 17 November 2023)

We report the observation of the anisotropic magneto-Thomson effect (AMTE), which is one of the higher-order thermoelectric effects in a ferromagnet. Using lock-in thermography, we demonstrated that in a ferromagnetic NiPt alloy, the cooling or heating induced by the Thomson effect depends on the angle between the magnetization direction and the temperature gradient or charge current applied to the alloy. AMTE observed here is the missing ferromagnetic analog of the magneto-Thomson effect in a nonmagnetic conductor, providing the basis for nonlinear spin caloritronics and thermoelectrics.

DOI: 10.1103/PhysRevLett.131.206701

In the 19th century, the Seebeck (Peltier) effect was discovered, which refers to the generation of a charge (heat) current in linear response to a heat (charge) current applied to a conductor. Over the past decades, various materials and physical mechanisms have been investigated for achieving good thermoelectric properties, and the Seebeck and Peltier effects are recognized as key technologies to solve environmental issues [1,2]. In addition to these linear-response thermoelectric effects, the Thomson effect was predicted by William Thomson [3,4]. The Thomson effect refers to the heat release or absorption as a result of a charge current  $\mathbf{I}$  applied to a conductor under a temperature gradient  $\nabla T$ , where  $\nabla T \parallel \mathbf{I}$ . The Thomson effect enables electronic cooling in a single material without junction structures, which cannot be realized by the conventional Peltier effect [5]. The heat production rate per unit volume due to the Thomson effect is expressed as

$$\dot{q} = -\tau \mathbf{j}_c \cdot \nabla T, \quad (1)$$

where  $\tau$  and  $\mathbf{j}_c$  are the Thomson coefficient and charge current density, respectively.  $\tau$  is related to Seebeck coefficient  $S$  and Peltier coefficient  $\Pi$  through the first and second Thomson relations, and can be expressed as

$$\tau = \frac{d\Pi}{dT} - S = T \frac{dS}{dT}, \quad (2)$$

where  $T$  represents the absolute temperature [6–8]. Because  $\dot{q}$  is proportional to both  $\mathbf{j}_c$  and  $\nabla T$  and determined by the temperature derivative of  $S$ , the Thomson effect is classified as a non-linear thermoelectric effect (note that  $S$  is assumed to be temperature- or position-independent in a material in the linear-response thermoelectric effects).

With the recent development of spin caloritronics [9–11], various linear-response magneto-thermoelectric effects have been discovered in magnetic materials. Such phenomena

include the anisotropic magneto-Seebeck effect (AMSE) [anisotropic magneto-Peltier effect (AMPE)], in which  $S$  ( $\Pi$ ) of a magnetic material depends on the direction of the magnetization  $\mathbf{M}$  due to the concerted action of the spin-polarized electron transport and spin-orbit interaction [12–19]. Owing to the unique symmetry and active control of thermoelectric conversion through  $\mathbf{M}$  manipulation, these magneto-thermoelectric phenomena offer several advantages over conventional thermoelectric phenomena. However, nonlinear magneto-thermoelectric effects in magnetic materials had long been unobserved.

This situation is being gradually changed by the recent observation of the magneto-Thomson effect in a non-magnetic conductor [20] and the giant Thomson effect in magnetic phase-transition materials [21], which has provided a new avenue for investigating various nonlinear magneto-thermoelectric effects. Equation (2) suggests that, in a similar manner to AMSE and AMPE,  $\tau$  and the resultant Thomson-effect-induced cooling or heating depend on the direction of  $\mathbf{M}$  in a magnetic material (Fig. 1): this is an anisotropic magneto-Thomson effect (AMTE), in which  $\Delta\tau \equiv T (d\Delta S/dT)$  is finite. Here,  $\Delta\tau = \tau_{\parallel} - \tau_{\perp}$  denotes the anisotropy of  $\tau$  with  $\tau_{\parallel}$  ( $\tau_{\perp}$ ) being the Thomson coefficient in the  $\nabla T \parallel \mathbf{I} \parallel \mathbf{M}$  ( $\nabla T \parallel \mathbf{I} \perp \mathbf{M}$ ) configuration, while  $\Delta S = S_{\parallel} - S_{\perp}$  the anisotropy of  $S$  with  $S_{\parallel}$  ( $S_{\perp}$ ) being the Seebeck coefficient in the  $\nabla T \parallel \mathbf{M}$  ( $\nabla T \perp \mathbf{M}$ ) configuration. Importantly, the origin of AMTE is different from that of the conventional magneto-Thomson effect in a nonmagnetic conductor; AMTE is attributable to the intrinsic electronic structure through the spin-orbit interaction [15], while the conventional magneto-Thomson effect is due to the simple Lorentz force acting on conduction carriers [20]. However, the observation of AMTE is yet to be realized; AMTE is the missing piece of the nonlinear magneto-thermoelectric effects in magnetic materials.

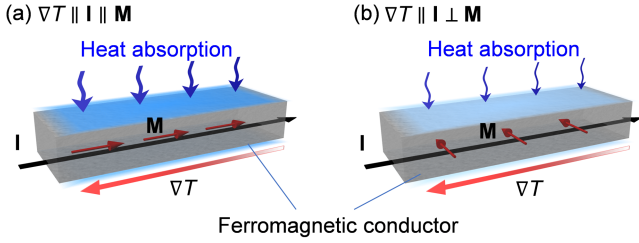


FIG. 1. Schematics of the cooling induced by the anisotropic magneto-Thomson effect in the  $\nabla T \parallel \mathbf{I} \parallel \mathbf{M}$  (a) and  $\nabla T \parallel \mathbf{I} \perp \mathbf{M}$  (b) configurations. When a charge current  $\mathbf{I}$  and a temperature gradient  $\nabla T$  are applied to a ferromagnetic conductor, the magnitude of the Thomson-effect-induced cooling or heating depends on the direction of the spontaneous magnetization  $\mathbf{M}$  due to the spin-orbit interaction acting on spin-polarized conduction carriers.

Herein, we report the observation of AMTE in a ferromagnetic metal. We experimentally demonstrated that the Thomson-effect-induced temperature change can be modulated by changing the  $\mathbf{M}$  direction. We used a polycrystalline  $\text{Ni}_{95}\text{Pt}_5$  alloy because it had a large  $T$ -dependent  $\Delta S$  [22], which satisfied the requirements for the appearance of AMTE. To observe the AMTE-induced temperature modulation, we employed a recently developed measurement method for the Thomson-effect-induced temperature change [20] based on lock-in thermography (LIT) [17,23–25]. We found that the  $\mathbf{M}$  dependence of the Thomson-effect-induced temperature change in the  $\text{Ni}_{95}\text{Pt}_5$  alloy in the  $\nabla T \parallel \mathbf{I} \parallel \mathbf{M}$  configuration was opposite in sign to that in the  $\nabla T \parallel \mathbf{I} \perp \mathbf{M}$  configuration. We further confirmed that the magnitude of the AMTE-induced signal for the  $\nabla T \parallel \mathbf{I} \parallel \mathbf{M}$  configuration was twice larger than that for the  $\nabla T \parallel \mathbf{I} \perp \mathbf{M}$  configuration. These results are consistent with the behaviors of the anisotropic magnetoresistance (AMR), AMSE, and AMPE in ferromagnetic conductors [11–19,26,27]. The observation of AMTE and demonstration of its functionality provide a new direction in condensed matter physics, magnetics, spin caloritronics, and thermoelectrics.

To determine the appropriate temperature for the observation of AMTE, we first estimated  $\Delta\tau$  in the  $\text{Ni}_{95}\text{Pt}_5$  alloy via the measurement of the  $T$  dependence of  $S$  and the Thomson relations (see Secs. S1 and S2 in the Supplemental Material [28] for details about the sample preparation and measurement method). Figure 2(a) shows  $T$  dependence of  $S$  for the  $\text{Ni}_{95}\text{Pt}_5$  slab measured under magnetic fields of  $|\mu_0 H| = 0$  (gray squares) and 800 mT (black circles) for the  $\nabla T \perp \mathbf{M}$  configuration, where  $\mu_0$  is the vacuum permeability. The measurement configuration is depicted in the inset of Fig. 2(a). The  $\tau$  values were calculated from the experimentally observed  $T$  dependence of  $S$  based on Eq. (2) and shown as independent data points in Fig. 2(b). The  $\tau$  values clearly show the  $|\mu_0 H|$  dependence suggesting the existence of the

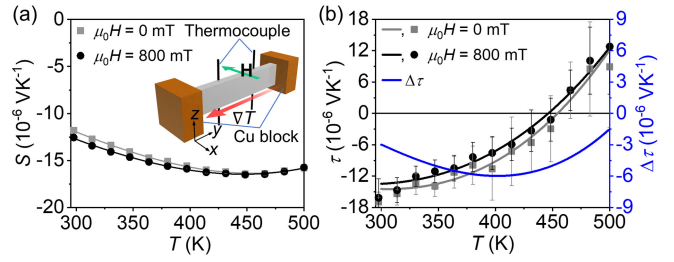


FIG. 2. (a) Temperature  $T$  dependence of the Seebeck coefficient  $S$  for the  $\text{Ni}_{95}\text{Pt}_5$  slab under external magnetic fields of  $|\mu_0 H| = 0$  (gray squares) and 800 mT (black circles) in the  $\nabla T \perp \mathbf{H}$  configuration.  $\mathbf{H}$  denotes the magnetic field with the magnitude  $H$ . The independent data points represent the experimental data, and the solid lines represent the fitting results obtained using 3rd-order polynomial functions. The error bars represent the standard deviations of the data during six consecutive measurements. (b)  $T$  dependence of the Thomson coefficient  $\tau$  estimated from Eq. (2) using the experimental data points (gray squares and black circles) and the polynomial fitted curves in (a) (gray and black curves). The blue curve represents the  $T$  dependence of the anisotropy of the Thomson coefficient  $\Delta\tau = 3(\tau_{0 \text{ mT}} - \tau_{800 \text{ mT}})$ , where  $\tau_{0 \text{ mT}}$  ( $\tau_{800 \text{ mT}}$ ) represents the value of  $\tau$  at 0 mT (800 mT) in the  $\nabla T \perp \mathbf{H}$  configuration.

magneto-Thomson effect but are scattered, making quantitative discussions difficult. Hence, we interpolated the experimentally observed  $T$ -dependent  $S$  data in Fig. 2(a) using a 3rd-order polynomial function and estimated the  $T$  dependence of  $\tau$  using Eq. (2) [see solid curves in Figs. 2(a) and 2(b)]. The  $T$  dependence of  $\Delta\tau$  is estimated by assuming the relation  $\Delta\tau = 3(\tau_{0 \text{ mT}} - \tau_{800 \text{ mT}})$  in the same manner as AMR and  $\Delta S$ , where  $\tau_{0 \text{ mT}}$  ( $\tau_{800 \text{ mT}}$ ) represents  $\tau$  at 0 mT (800 mT) for the  $\nabla T \perp \mathbf{M}$  configuration [see the blue curve in Fig. 2(b)]. Based on this estimation, we can expect that  $\Delta\tau$  increases with  $T$ , reaches its maximum value at  $\sim 400$  K, and then decreases with a further increase in  $T$ . Since no AMTE signal was observed in a  $\text{Ni}_{95}\text{Pt}_5$  alloy at room temperature within the margin of experimental errors in a previous attempt by Uchida *et al.* [20], we performed measurements at  $\sim 400$  K, where a large  $\Delta\tau$  and resultant AMTE-induced temperature modulation are expected to appear in this alloy.

To directly observe the AMTE-induced temperature change in the  $\text{Ni}_{95}\text{Pt}_5$  alloy, we used a thermoelectric imaging technique based on LIT [20]. Before the investigation of AMTE, we focused on the experiments in the absence of a magnetic field and validated the effectiveness of the LIT-based method for the measurement of the Thomson effect at high temperatures. Figure 3(a) shows a schematic of the experimental setup. A bar-shaped  $\text{Ni}_{95}\text{Pt}_5$  slab bridged two heat baths where chip heaters with a resistance of  $300 \Omega$  were attached to control the temperatures (see Sec. S3 in the Supplemental Material [28] for details). Hereinafter,  $P_{L(R)}$  denotes the power applied to the left (right) heater to increase the base temperature and

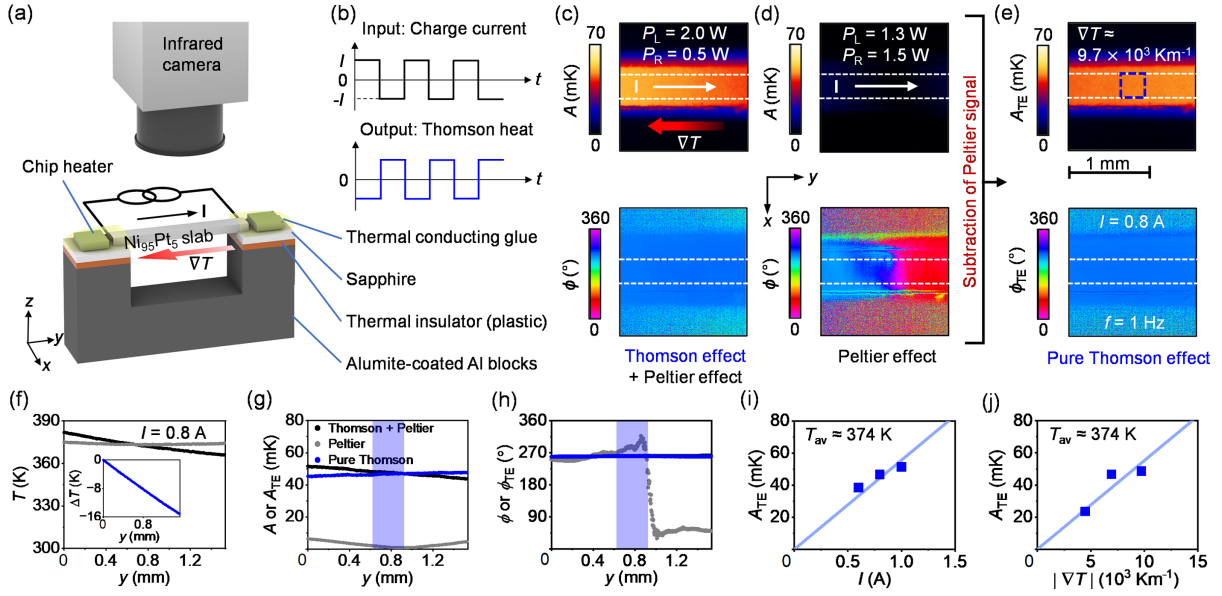


FIG. 3. (a) Schematic of the experimental configuration for the measurements of the Thomson effect in the  $\text{Ni}_{95}\text{Pt}_5$  slab using LIT. (b) Time ( $t$ ) chart of the charge current applied to the sample and the resultant Thomson-effect-induced heat. During the measurement, a square-wave-modulated alternating charge current with amplitude  $I$ , frequency  $f$ , and zero offset was applied to the slab. (c) Lock-in amplitude  $A$  and phase  $\phi$  images for the  $\text{Ni}_{95}\text{Pt}_5$  slab at  $I = 0.8$  A and  $f = 1.0$  Hz, measured with a left (right) heater power of  $P_L = 2.0$  W ( $P_R = 0.5$  W). (d)  $A$  and  $\phi$  images, measured with a left (right) heater power of  $P_L = 1.3$  W ( $P_R = 1.5$  W). (e)  $A_{TE}$  and  $\phi_{TE}$  images for the  $\text{Ni}_{95}\text{Pt}_5$  slab, obtained by subtracting the images in (d) from those in (c). (f)–(h) The  $y$ -directional steady-state temperature  $T$  (f),  $A$  or  $A_{TE}$  (g), and  $\phi$  or  $\phi_{TE}$  (h) profiles for the images shown in (c)–(e). The profiles were obtained by averaging 100  $y$ -directional profiles along the  $x$  direction; the averaged area is marked by white dotted lines. The Joule heating in the sample uniformly increases  $T$  by  $\sim 2$  K but does not affect the estimation of  $\nabla T$ . (i)  $I$  dependence of  $A_{TE}$  at  $\nabla T \approx 9.7 \times 10^3 \text{ Km}^{-1}$ . (j)  $|\nabla T|$  dependence of  $A_{TE}$  at  $I = 1.0$  A. The data points in (i) and (j) were obtained by averaging the  $A_{TE}$  values in the area indicated by the blue square with a size of  $100 \times 100$  pixels ( $0.3 \times 0.3$  mm) in (e).

generate  $\nabla T$ . The average base temperature of the sample was increased to  $T_{av} \approx 374$  K and a steady temperature gradient  $\nabla T$  was generated along the  $y$  direction by applying a charge current to the heaters. During LIT measurements of the Thomson effect, a square-wave-modulated alternating charge current with amplitude  $I$ , frequency  $f$ , and zero offset was applied to the sample along the  $y$  direction in the presence of  $\nabla T$  [see Fig. 3(b)]. Under this condition, we recorded thermal images of the surface of the  $\text{Ni}_{95}\text{Pt}_5$  slab using an infrared camera and extracted the temperature change oscillating with the same frequency as the current through Fourier analysis. This analysis allowed us to separate the contribution of thermoelectric effects ( $\propto I$ ) from that of Joule heating ( $\propto I^2$ ), because the Joule heating generated by such a square-wave-modulated alternating current is constant in time [17,25]. The obtained thermal images were transformed into lock-in amplitude  $A$  and phase  $\phi$  images, where  $A$  represents the magnitude of the current-induced temperature change and  $\phi$  indicates the sign and time delay of the temperature change. In this experimental configuration, the measured LIT images may include contributions from not only the Thomson effect but also the Peltier effect generated at the ends of the sample connected to electrical leads. To estimate the contribution of the Peltier effect, LIT images in the absence of  $\nabla T$  were also measured.

Figure 3(c) shows the  $A$  and  $\phi$  images for the  $\text{Ni}_{95}\text{Pt}_5$  slab at  $I = 0.8$  A,  $f = 1.0$  Hz, and  $P_{L(R)} = 2.0$  W (0.5 W), where the left side of the sample was hotter and large  $\nabla T$  was generated along the  $y$ -direction. Charge-current-induced temperature modulation was clearly observed in the presence of  $\nabla T$ . Figure 3(d) shows the images for the same  $\text{Ni}_{95}\text{Pt}_5$  slab measured with the application of a comparable  $P_{L(R)}$ , where the average base temperature was almost identical to that in Fig. 3(c) but  $\nabla T$  was negligible [Fig. 3(f)]. In the absence of  $\nabla T$ , we observed small but finite background signals due to the Peltier effect [see Fig. 3(d) and note that the sign of the Peltier-effect-induced temperature modulation is reversed between the ends of the sample, inducing the sudden phase change by  $\sim 180^\circ$  around the center]. By subtracting the background signal in Fig. 3(d) from the signal in Fig. 3(c), we obtained the  $A_{TE}$  and  $\phi_{TE}$  images in Fig. 3(e). The signals in these images are attributed entirely to the Thomson effect; hereafter, we focus on the subtracted images. The  $y$ -directional line profiles of  $T$ ,  $A$ , or  $A_{TE}$ , and  $\phi$  or  $\phi_{TE}$  for the images in Figs. 3(c)–3(e) are shown in Figs. 3(f)–3(h). The applied magnitude of  $\nabla T$  was estimated to be  $9.7 \times 10^3 \text{ Km}^{-1}$  by fitting the steady-state temperature difference  $\Delta T$  profile in Fig. 3(f) with a linear function. Figures 3(i) and 3(j) present the average  $A_{TE}$  values in the blue square region with

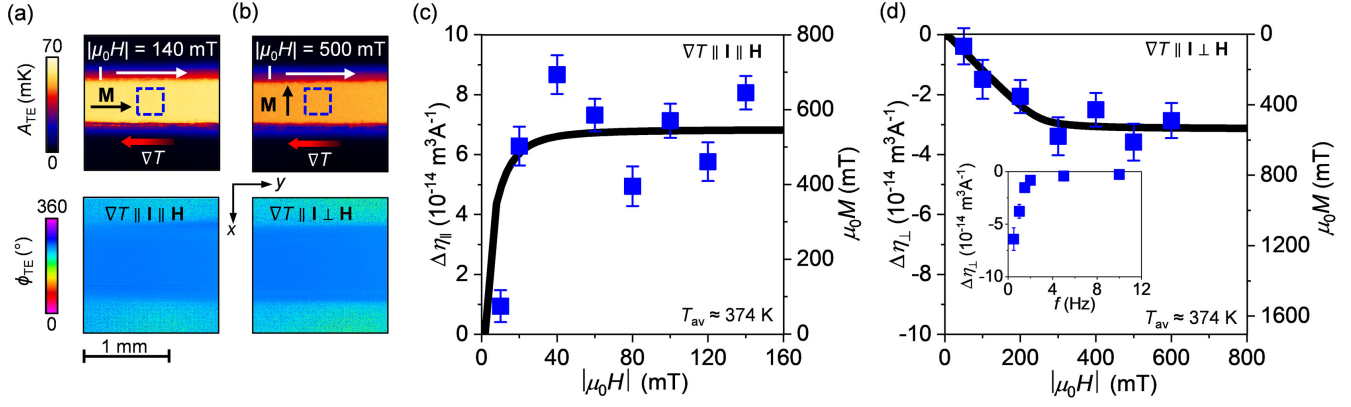


FIG. 4. (a),(b)  $A_{TE}$  and  $\phi_{TE}$  images for the  $Ni_{95}Pt_5$  slab at  $I = 1.0$  A and  $f = 1.0$  Hz, measured when a magnetic field of  $|\mu_0 H| = 140$  mT and  $\nabla T \approx 9.2 \times 10^3 \text{ Km}^{-1}$  were applied in the  $\nabla T \parallel \mathbf{I} \parallel \mathbf{H}$  configuration (a) and  $|\mu_0 H| = 500$  mT and  $\nabla T \approx 10.1 \times 10^3 \text{ Km}^{-1}$  were applied in the  $\nabla T \perp \mathbf{I} \perp \mathbf{H}$  configuration (b). (c),(d)  $|\mu_0 H|$  dependence of  $\Delta\eta_{\parallel}$  and  $\Delta\eta_{\perp}$  for the  $Ni_{95}Pt_5$  slab in the  $\nabla T \parallel \mathbf{I} \parallel \mathbf{H}$  and  $\nabla T \perp \mathbf{I} \perp \mathbf{H}$  configurations. In the  $\nabla T \parallel \mathbf{I} \parallel \mathbf{H}$  ( $\nabla T \perp \mathbf{I} \perp \mathbf{H}$ ) configuration, we define  $\Delta\eta_{\parallel(\perp)}(|H|) = \eta_{\parallel(\perp)}(|H|) - \eta_{\parallel(\perp)}(0 \text{ mT})$  with  $\eta_{\parallel(\perp)} = |A_{TE}/(j_c \nabla T)|$  and  $j_c$  being the square-wave amplitude of the charge current density. The inset in (d) shows the  $f$  dependence of  $\Delta\eta_{\perp}$ . The data points in (c) and (d) were obtained by averaging the  $A_{TE}$  values in the areas indicated by the blue squares with sizes of  $100 \times 100$  pixels ( $0.3 \times 0.3$  mm) in (a) and (b), respectively. The error bars represent the standard deviations of the data in the corresponding squares.

respect to  $I$  and  $\nabla T$ , respectively. The magnitude of the  $A_{TE}$  signal increased in proportion to  $I$  and  $\nabla T$  applied to the  $Ni_{95}Pt_5$  slab. These behaviors are consistent with the features of the Thomson effect [20,21], validating our measurement method at the high temperature ( $T_{av} \approx 374$  K).

Next, we investigated AMTE in the  $Ni_{95}Pt_5$  alloy. For the demonstration, we performed the same LIT measurements with an applied external magnetic field under the configurations of  $\nabla T \parallel \mathbf{I} \parallel \mathbf{H}$  and  $\nabla T \perp \mathbf{I} \perp \mathbf{H}$ , where  $\mathbf{H}$  was along the  $y$  and  $x$  directions, respectively. Figures 4(a) and 4(b) show the  $A_{TE}$  and  $\phi_{TE}$  images at  $I = 1.0$  A and  $f = 1.0$  Hz in the presence of  $\mathbf{H}$  with  $|\mu_0 H| = 140$  mT for the  $\nabla T \parallel \mathbf{I} \parallel \mathbf{M}$  configuration and  $|\mu_0 H| = 500$  mT for the  $\nabla T \perp \mathbf{I} \perp \mathbf{M}$  configuration, where  $\nabla T \approx 9.2 \times 10^3$  and  $10.1 \times 10^3 \text{ Km}^{-1}$ , respectively. Here,  $\mathbf{M}$  of the  $Ni_{95}Pt_5$  slab was saturated under the applied  $|\mu_0 H|$  for both configurations [Figs. 4(c) and 4(d)]. To obtain the pure Thomson contribution in the presence of  $\mathbf{H}$ , we used a previously reported procedure for the magneto-Thomson effect [20]. As shown in Figs. 4(a) and 4(b), the magnitude of the temperature modulation due to the Thomson effect varied with respect to the direction of  $\mathbf{H}$  or  $\mathbf{M}$ ; even though larger  $\nabla T$  was applied for the data in Fig. 4(b), the magnitude of the  $A_{TE}$  signal in Fig. 4(b) is smaller than that in Fig. 4(a). We then systematically measured the  $|\mu_0 H|$  dependence of the  $A_{TE}$  signal, where we applied different values of  $|\mu_0 H| \leq 140$  mT for the  $\nabla T \parallel \mathbf{I} \parallel \mathbf{H}$  configuration and  $|\mu_0 H| \leq 600$  mT for the  $\nabla T \perp \mathbf{I} \perp \mathbf{H}$  configuration. The  $|\mu_0 H|$  dependence of the  $A_{TE}$  signal can be compared in terms of  $\eta_{\parallel}(\eta_{\perp}) = |A_{TE}/(j_c \nabla T)|$  for the  $\nabla T \parallel \mathbf{I} \parallel \mathbf{H}$  ( $\nabla T \perp \mathbf{I} \perp \mathbf{H}$ ) configuration [20], where  $j_c$  represents the square-wave amplitude of the charge current density. The  $|\mu_0 H|$ -dependent change of the Thomson signal for the  $\nabla T \parallel \mathbf{I} \parallel \mathbf{H}$  ( $\nabla T \perp \mathbf{I} \perp \mathbf{H}$ ) configuration  $\Delta\eta_{\parallel}$

( $\Delta\eta_{\perp}$ ) was estimated by subtracting the  $\eta_{\parallel}$  ( $\eta_{\perp}$ ) values at  $|\mu_0 H| = 0$  mT from those at  $|\mu_0 H| > 0$  mT. Figures 4(c) and 4(d) show  $\Delta\eta_{\parallel}$  and  $\Delta\eta_{\perp}$ , respectively, as a function of  $|\mu_0 H|$  at  $f = 1.0$  Hz. Here, we selected  $f = 1.0$  Hz for the subsequent demonstration because of its good signal-to-noise ratio [see also the  $f$  dependence of  $\Delta\eta_{\perp}$  at  $|\mu_0 H| = 500$  mT shown in the inset of Fig. 4(d)]. We note that the observed  $|\mu_0 H|$  dependence of  $\Delta\eta_{\parallel}$  is more scattered than that of  $\Delta\eta_{\perp}$  due to the difference in thermal stability (see Sec. S3 in the Supplemental Material [28]). However, the overall behaviors of the  $\Delta\eta_{\parallel}$  and  $\Delta\eta_{\perp}$  signals can be clearly confirmed from this data; the magnitude of the signals first monotonically increased with an increase in  $|\mu_0 H|$  and remained almost constant after the saturation of  $\mathbf{M}$  following the  $M$ - $H$  curve of the  $Ni_{95}Pt_5$  slab in each configuration (see Sec. S4 in the Supplemental Material [28] for details about the magnetization measurement). This tendency is similar to AMSE and AMPE in a ferromagnet [17], and differs from the magneto-Thomson effect in the nonmagnetic conductor under an external magnetic field [20], where the magnitude of the temperature modulation was not saturated with an increase in  $|\mu_0 H|$ . Importantly, the magnitude of the saturated  $\Delta\eta_{\parallel}$  signal was twice that of the saturated  $\Delta\eta_{\perp}$  [compare Figs. 4(c) and 4(d)]. This behavior is also consistent with that of AMSE and AMPE in isotropic ferromagnetic conductors [13–19], confirming the existence of AMTE. The magnitude of the  $\Delta\eta_{\parallel} - \Delta\eta_{\perp}$  value was estimated to be  $\sim 1 \times 10^{-13} \text{ m}^3 \text{ A}^{-1}$  for the  $Ni_{95}Pt_5$  alloy at  $T_{av} \approx 374$  K, which is approximately 20% of  $\eta$  in the absence of  $\mathbf{H}$ . We confirmed that the sign of the  $\mathbf{M}$ -dependent change in the  $A_{TE}$  signal in the  $Ni_{95}Pt_5$  alloy was consistent with the prediction based on the data in

Fig. 2, supporting our interpretation that the observed behavior is due to AMTE. As shown in Fig. S1 in the Supplemental Material [28], we also observed a similar AMTE signal at a lower temperature and found that the magnitude of the AMTE signal at  $\sim 330$  K is smaller than that at  $\sim 374$  K, consistent with the prediction in Fig. 2(b).

In conclusion, we realized the direct observation of AMTE in a polycrystalline  $\text{Ni}_{95}\text{Pt}_5$  alloy using the LIT technique. The magnitude of the Thomson-effect-induced temperature change in the  $\text{Ni}_{95}\text{Pt}_5$  alloy was modulated by changing the  $\mathbf{M}$  direction; the change ratio between the  $\nabla T \parallel \mathbf{I} \parallel \mathbf{M}$  and  $\nabla T \parallel \mathbf{I} \perp \mathbf{M}$  configurations reached  $\sim 20\%$  at  $\sim 374$  K. AMTE observed here suggests the possibility of the active modulation of thermoelectric cooling or heating power in a single material without junctions through the manipulation of  $\mathbf{M}$ . If the  $\mathbf{M}$  direction is properly defined by magnetic anisotropy, AMTE can occur even in the absence of a magnetic field; this is a crucial difference from the conventional magneto-Thomson effect in non-magnetic conductors, providing a new concept of thermal energy engineering using nonlinear magnetothermoelectric effects [5]. However, for applications, the magnitude and efficiency of AMTE must be significantly enhanced through material investigation and device optimization. For the realization of giant AMTE, investigating ferromagnets with large  $\Delta\tau$  values through data-driven material informatics, appropriate band engineering, and first-principles prediction focusing on the  $\Delta\tau$  parameter are potential strategies. Thus, the observation of AMTE will invigorate materials science and physics research in nonlinear spin caloritronics and thermoelectrics.

The authors thank R. Iguchi, K. Masuda, and Y. Miura for valuable discussions. This work was supported by Grant-in-Aid for Scientific Research (B) (Grant No. 19H02585) and Grant-in-Aid for Scientific Research (S) (Grant No. 22H04965) from JSPS KAKENHI, Japan, CREST “Creation of Innovative Core Technologies for Nano-enabled Thermal Management” (Grant No. JPMJCR17I1) and ERATO “Magnetic Thermal Management Materials” (Grant No. JPMJER2201) from JST, Japan. R. M. was supported by JSPS Postdoctoral Fellowship for Research in Japan (Standard) from JSPS, Japan (Grant No. P21064).

\*Corresponding author: MODAK.Rajkumar@nims.go.jp

†Corresponding author: UCHIDA.Kenichi@nims.go.jp

- [1] G. D. Mahan, Good thermoelectrics, in *Solid State Physics—Advances in Research and Applications* (Academic Press, New York, 1998), Vol. 51, p. 81.
- [2] X. Zhang and L.-D. Zhao, *J. Mater.* **1**, 92 (2015).
- [3] W. Thomson, *Trans. R. Soc. Edinburgh* **21**, 123 (1857).

- [4] W. Thomson, *Proc. R. Soc. Edinburgh* **3**, 91 (1857).
- [5] T. Chiba, R. Iguchi, T. Komine, Y. Hasegawa, and K. Uchida, *Jpn. J. Appl. Phys.* **62**, 037001 (2023).
- [6] R. Wolfe and G. E. Smith, *Phys. Rev.* **129**, 1086 (1963).
- [7] Y. Apertet and C. Goupil, *Int. J. Therm. Sci.* **104**, 225 (2016).
- [8] A. M. Steane, *Thermodynamics* (Oxford University Press, Oxford, 2016).
- [9] G. E. W. Bauer, E. Saitoh, and B. J. van Wees, *Nat. Mater.* **11**, 391 (2012).
- [10] S. R. Boona, R. C. Myers, and J. P. Heremans, *Energy Environ. Sci.* **7**, 885 (2014).
- [11] K. Uchida, *Proc. Jpn. Acad. Ser. B* **97**, 69 (2021).
- [12] J.-E. Wegrowe, Q. A. Nguyen, M. Al-Barki, J.-F. Dayen, T. L. Wade, and H.-J. Drouhin, *Phys. Rev. B* **73**, 134422 (2006).
- [13] A. D. Avery, M. R. Pufall, and B. L. Zink, *Phys. Rev. Lett.* **109**, 196602 (2012).
- [14] M. Schmid, S. Srichandan, D. Meier, T. Kuschel, J.-M. Schmalhorst, M. Vogel, G. Reiss, C. Strunk, and C. H. Back, *Phys. Rev. Lett.* **111**, 187201 (2013).
- [15] K. S. Das, F. K. Dejene, B. J. van Wees, and I. J. Vera-Marun, *Phys. Rev. B* **94**, 180403(R) (2016).
- [16] O. Reimer, D. Meier, M. Bovender, L. Helmich, J.-O. Dreessen, J. Krieff, A. S. Shestakov, C. H. Back, J.-M. Schmalhorst, A. Hütten, G. Reiss, and T. Kuschel, *Sci. Rep.* **7**, 40586 (2017).
- [17] K. Uchida, S. Daimon, R. Iguchi, and E. Saitoh, *Nature (London)* **558**, 95 (2018).
- [18] K. Masuda, K. Uchida, R. Iguchi, and Y. Miura, *Phys. Rev. B* **99**, 104406 (2019).
- [19] A. Miura, R. Iguchi, T. Seki, K. Takanashi, and K. Uchida, *Phys. Rev. Mater.* **4**, 034409 (2020).
- [20] K. Uchida, M. Murata, A. Miura, and R. Iguchi, *Phys. Rev. Lett.* **125**, 106601 (2020).
- [21] R. Modak, M. Murata, D. Hou, A. Miura, R. Iguchi, B. Xu, R. Guo, J. Shiomi, Y. Sakuraba, and K. Uchida, *Appl. Phys. Rev.* **9**, 011414 (2022).
- [22] T. Hirai, R. Modak, A. Miura, T. Seki, K. Takanashi, and K. Uchida, *Appl. Phys. Express* **14**, 073001 (2021).
- [23] O. Breitenstein, W. Warta, and M. Langenkamp, *Lock-in Thermography: Basics and Use for Evaluating Electronic Devices and Materials* (Springer, Berlin, Heidelberg, 2010).
- [24] O. Wid, J. Bauer, A. Müller, O. Breitenstein, S. S. P. Parkin, and G. Schmidt, *Sci. Rep.* **6**, 28233 (2016).
- [25] S. Daimon, R. Iguchi, T. Hioki, E. Saitoh, and K. Uchida, *Nat. Commun.* **7**, 13754 (2016).
- [26] R. M. Bozorth, *Phys. Rev.* **70**, 923 (1946).
- [27] T. McGuire and R. Potter, *IEEE Trans. Magn.* **11**, 1018 (1975).
- [28] See Supplemental Material at <http://link.aps.org/supplemental/10.1103/PhysRevLett.131.206701> for further details regarding the sample preparation and measurement procedures.